Acta Materialia 223 (2022) 117468

Contents lists available at ScienceDirect

Acta Materialia

journal homepage: www.elsevier.com/locate/actamat

# Room-temperature deformation of single crystals of transition-metal disilicides ($TMSi_2$) with the $C11_b$ (TM = Mo) and C40 (TM = V, Cr, Nb and Ta) structures investigated by micropillar compression

Kyosuke Kishida[a,b,*], Satoshi Nakatsuka[a], Hiroaki Nose[a], Haruyuki Inui[a,b]

[a] Department of Materials Science and Engineering, Kyoto University, Sakyo-ku, Kyoto 606-8501, Japan
[b] Center for Elements Strategy Initiative for Structural Materials, Kyoto University, Sakyo-ku, Kyoto 606-8501, Japan

ARTICLE INFO

*Article history:*
Received 27 July 2021
Revised 3 November 2021
Accepted 4 November 2021
Available online 7 November 2021

*Keywords:*
Transition metal silicides
Deformation structure
Dislocations
Mechanical properties
Micropillar compression

ABSTRACT

The room-temperature deformation behavior of single crystals of transition-metal (TM) disilicides with the tetragonal $C11_b$ (TM=Mo) and hexagonal C40 (TM = V, Cr, Nb and Ta) structures has been investigated by micropillar compression as a function of specimen size, paying special attention to the deformation behavior of the equivalent slip ($\{110\}\langle\bar{1}11\rangle$ and $(0001)\langle 2\bar{1}\bar{1}0\rangle$, respectively for the two structures). In contrast to bulk single crystals, in which high temperature at least exceeding 400 °C is usually needed for the operation of the equivalent slip, plastic flow is observed by the operation of the equivalent slip at room temperature for all these TM disilicides in the micropillar form. The critical resolved shear stress (CRSS) value exhibits the 'smaller is stronger' behavior following an inverse power-law relationship for all these TM disilicides. The bulk CRSS values at room temperature estimated from the specimen size dependence are 620 ± 40, 240 ± 20, 1,440 ± 10, 640 ± 20 and 1,300 ± 30 MPa for $MoSi_2$, $VSi_2$, $CrSi_2$, $NbSi_2$ and $TaSi_2$, respectively. Transmission electron microscopy reveals that the equivalent slip at room temperature occurs by a conventional shear mechanism for all TM disilicides, indicating the change in deformation mechanism from synchroshear in bulk to conventional shear in micropillars occurs in $CrSi_2$ with decreasing temperature.



## 1. Introduction

Transition-metal (TM) disilicides with the tetragonal $C11_b$ and hexagonal C40 structures have been considered as candidate materials for ultra-high temperature structural applications because of their excellent properties such as high melting points around 2000 °C, high strength, good oxidation resistance at high temperatures and relatively low densities [1–5]. However, extensive studies made during the past three decades have revealed that low ductility and fracture toughness at ambient temperatures can be serious drawbacks for their practical applications [1–5]. Mo and W are known to form TM disilicides with the tetragonal $C11_b$ structure, while V, Cr, Nb and Ta form TM disilicides with the hexagonal C40 structure. Although these two structures look quite differently at a first glance (Fig. 1a and b), these structures can be generated by changing the stacking sequence of the hexagonally-arranged $TMSi_2$ stoichiometric atomic plane (Fig. 1c). The $TMSi_2$ stoichiometric atomic plane corresponds to (110) in the tetragonal $C11_b$ structure and (0001) in the hexagonal C40 structure (Fig. 1a and b). The atomic arrangement on (110) in the tetragonal $C11_b$ structure can be regarded as regular hexagonal as in (0001) in the hexagonal C40 structure, if the $c/a$ axial ratio of the $C11_b$ structure is idealistically $6^{1/2}$. Indeed, the $c/a$ axial ratio (2.452) of $MoSi_2$ is very close to the ideal value of $6^{1/2}$. There are four equivalent positions, A–D (Fig. 1c) for stacking hexagonally-arranged $TMSi_2$ stoichiometric atomic planes if transition metals occupy saddle positions directly above Si-Si bonds in their stacking [2]. The $C11_b$ and C40 structures are generated based on the AB and ABC[1] stacking of these $TMSi_2$ stoichiometric atomic planes, respectively [2]. Then, $\langle\bar{1}11\rangle$ directions on {110} of the $C11_b$ structure are parallel to the $\langle 2\bar{1}\bar{1}0\rangle$ directions on (0001) in the C40 structure (Fig. 1c). This in-

* Corresponding author at: Department of Materials Science and Engineering, Kyoto University, Sakyo-ku, Kyoto 606-8501, Japan.
*E-mail address:* kishida.kyosuke.6w@kyoto-u.ac.jp (K. Kishida).

[1] The CBA stacking is also possible for the hexagonal C40 structure [6], so that the structure belongs to two enantiomorphic space groups of $P6_222$ and $P6_422$ [7–9]. In the present paper, only the C40 structure based on the ABC stacking is considered for the simplicity.

https://doi.org/10.1016/j.actamat.2021.117468

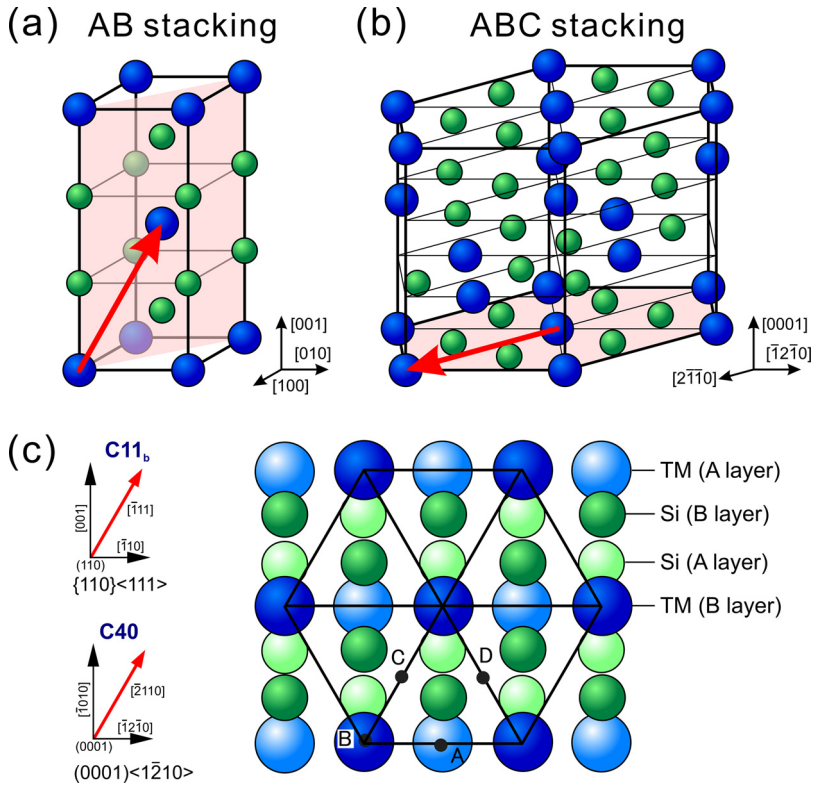


**Fig. 1.** (a) Tetragonal $C11_b$ and (b) hexagonal C40 crystal structures. (c) Atomic arrangement on the hexagonally-arranged $TMSi_2$ stoichiometric atomic plane corresponding to (110) in the tetragonal $C11_b$ structure and (0001) in the hexagonal C40 structure. Four equivalent positions, A–D for stacking the hexagonally-arranged $TMSi_2$ stoichiometric atomic planes are also indicated.

dicates that slip on {110}<$\bar{1}$11> in the $C11_b$ structure is equivalent to slip on (0001) $\langle 2\bar{1}\bar{1}0\rangle$ in the C40 structure.

Deformation experiments so far made on bulk single crystals of these $C11_b$ and C40 TM disilicides have indicated that these equivalent slip systems ({110}<$\bar{1}$11> and (0001) <$2\bar{1}\bar{1}0$>) indeed operate in all these $C11_b$ and C40 TM disilicides [10–20], although some high temperatures are generally needed for the equivalent slip systems to start to operate. In $MoSi_2$ with $C11_b$ structure, the onset temperature for plastic flow by the operation of the {110}<$\bar{1}$11> equivalent slip is 500 °C, while room-temperature plastic flow is possible even at room temperature when other slip systems such as {01$\bar{1}$}<331> and {011}<100> are operative [13]. On the other hand, while the (0001) $\langle 2\bar{1}\bar{1}0\rangle$ equivalent slip is the only operative slip system in all C40 TM disilicides, the onset temperatures for plastic flow by the operation of the equivalent slip are 400, 800, 500 and 600 °C, respectively for $VSi_2$, $CrSi_2$, $NbSi_2$ and $TaSi_2$ (Fig. S1a) [16–18,20]. High-resolution transmission electron microscopy (HRTEM) of the core structure for dislocations of the equivalent slip systems has confirmed that the equivalent slip in $MoSi_2$, $VSi_2$, $NbSi_2$ and $TaSi_2$ occurs in a conventional manner with two-coupled identical collinear partial dislocations, while that in $CrSi_2$ as well as isostructural $Mo(Si,Al)_2$ occurs in a special manner called synchroshear mechanism (Fig. S2; the detailed description for the two deformation mechanisms will be made in the Section 3.2) [16–20]. Of interest to note is that the difference in deformation mechanism (either conventional shear or synchroshear) is reflected in the difference in the onset temperature for plastic flow so that these five different TM disilicides are classified into two groups [20]. The low-temperature group, which consists of $MoSi_2$, $VSi_2$, $NbSi_2$ and $TaSi_2$, exhibits the onset temperature for plastic flow around 0.3 $T_m$ ($T_m$: melting temperature) and they deform by a conventional shear mechanism. On the other hand, the high temperature group, which consists of $CrSi_2$ and $Mo(Si,Al)_2$, exhibits the onset temperature around 0.6 $T_m$ and they deform by a synchroshear mechanism (Fig. S1b) [16,19,20]. In any sense, these high onset temperatures for plastic flow are one reason for low ductility and fracture toughness of these TM disilicides at ambient temperatures. It is thus very interesting to investigate the room-temperature deformation behaviors and dislocation activities of these TM disilicides, in order to find out ways to improve the poor ambient-temperature mechanical properties. Recently, micropillar compression tests have been increasingly recognized to be very useful for studying the deformation behavior of brittle materials such as Si, GaAs at temperatures far below their ductile to brittle transition temperatures for their bulk specimens [21–26]. We have systematically and successfully applied the micropillar compression method to various hard and brittle materials including TM silicides [27–30], TM borides [31], Fe-Zn intermetallics [32–35] FeCr sigma phase compound [36], $Ti_3SiC_2$ MAX phase compound [37], SiC [38] and so on to explore their room-temperature deformation behaviors without bothering specimen surface oxidation and dislocation climb, both of which usually occur at high temperatures making slip system identification difficult for bulk crystals.

In the present study, we investigate the plastic deformation behavior of single crystals of $C11_b$–$MoSi_2$ and C40-$TMSi_2$ (TM=V, Cr, Nb and Ta) at room temperature by micropillar compression as a function of specimen size ranging from 1 to 10 $\mu$m with the use of micropillar specimens favorably oriented for the operation of the equivalent slip system, in order to identify the actually operative slip systems and their critical resolved shear stresses (CRSS) at room temperature. Special attention is paid to deduce the deformation mechanism (either conventional shear or synchroshear) of the operative slip system by atomic-resolution scanning transmission electron microscopy, to see if any change occurs from that observed in the corresponding bulk single crystals deformed at high temperatures.

**Table 1**
The highest Schmid factor values for {110}<$\bar{1}$11> slip for $C11_b$-$MoSi_2$ and (0001)< $2\bar{1}\bar{1}0$> slip for C40-$VSi_2$, $CrSi_2$, $NbSi_2$ and $TaSi_2$ with the loading-axis orientations employed in the present study.

| | $MoSi_2$ | $VSi_2$ | $CrSi_2$ | $NbSi_2$ | $TaSi_2$ |
|---|---|---|---|---|---|
| Loading axis | [071] | [$2\bar{1}\bar{1}2$] | | | |
| Slip system | {110}<$\bar{1}$11> | (0001)< $2\bar{1}\bar{1}0$> | | | |
| Schmid factor | 0.414 | 0.499 | 0.500 | 0.497 | 0.498 |

## 2. Experimental procedure

Rod ingots of stoichiometric $TMSi_2$ (TM = Mo, V, Cr, Nb and Ta) were prepared by Ar arc-melting of high-purity elements. Single crystal rods of these $TMSi_2$ were grown by directional solidification using an optical floating-zone furnace at a growth rate of 10 mm/h under Ar gas flow. Crystal orientations of the single crystal rods were determined by the X-ray Laue back-reflection method. Oriented specimens were cut from the as-grown single crystal rods and their surfaces were mechanically polished and finished with diamond paste to mirror finish. Micropillar specimens with a square cross section having an edge length $L$ ranging from 1 to 10 $\mu$m and an aspect ratio of 1:2–1:3 were cut from the oriented specimens by the focused ion beam (FIB) technique. The compression-axis orientation investigated for $MoSi_2$ with the $C11_b$ structure was [071], while it was [$2\bar{1}\bar{1}2$], which is about 45 ° away from the c-axis, for $TMSi_2$ (TM=V, Cr, Nb and Ta) with the C40 structure. The largest Schmid factors for the equivalent slip systems ({110}<$\bar{1}$11> and (0001)[$2\bar{1}\bar{1}0$] slip, respectively for the $C11_b$ and C40 structures) are listed in Table 1 for each of $TMSi_2$. Micropillar compression tests were made with an Agilent Technologies Nano Indenter G200 nanomechanical tester equipped with a flat-punch diamond tip at room temperature under the displacement-rate-controlled mode at a nominal strain rate of $6 \times 10^{-4}$ $s^{-1}$. Microstructures of micropillar specimens before and after compression tests were examined by scanning electron microscopy (SEM) with a JEOL JSM-7001FA electron microscope in order to measure dimensions and analyze slip traces, respectively. Initial specimen height $H$ was obtained from its projected length $H$' measured in an SEM image taken along the direction inclined by 30 ° from the loading axis toward a side surface using the equation H = H'/sin30 ° with a measurement error of about 5%, which results in an error in strain evaluation of approximately 5%. Deformation microstructures developed in the deformed micropillars were also investigated by transmission electron microscopy (TEM) and scanning transmission electron microscopy (STEM) with JEOL JEM-2000FX, JEOL JEM-2100F and JEM-ARM200F electron microscopes operated at 200 kV. Specimens for TEM/STEM observations were prepared by the FIB-SEM *in-situ* lift-out technique using a FEI Quanta 3D 200i Dual-Beam system equipped with an Omniprobe nanomanipulator.

## 3. Results

### 3.1. Stress-strain behavior and slip trace observation

Typical stress-strain curves obtained for micropillar specimens with various specimen sizes are shown in Fig. 2(a–e), respectively for $MoSi_2$, $VSi_2$, $CrSi_2$, $NbSi_2$ and $TaSi_2$. All compression tests were interrupted before failure occurs for the ease of slip trace observations. Surprisingly, all TM disilicides exhibit plastic flow even at room temperature in the micropillar form, in contrast to the high onset temperature for plastic flow in the bulk form [13,16–18,20]. Arrows in Fig. 2(a–e) indicate yield points estimated either from the elastic limit or from the stress at which the first strain bust occurs. The yield stress thus estimated shows a tendency to increase with the decrease in the specimen size (edge length $L$) for all TM disilicides. For $MoSi_2$, all stress-strain curves exhibit a relatively smooth transition from elastic to plastic flow followed by a plastic flow region with a gradual decrease in work-hardening rate, and all the specimens plastically deform at least to more than 2% plastic strain without failure. In contrast, all micropillar specimens of C40 TM disilicides deform plastically at least more than 4% plastic strain without failure at room temperature regardless of specimen size. Load drops are repeatedly observed in the plastic flow region, indicative of discrete strain bursts, for $NbSi_2$ (Fig. 2d) and $TaSi_2$ (Fig. 2e), while a relatively smooth transition from elastic to plastic flow is observed for $VSi_2$ (Fig. 2b) and $CrSi_2$ (Fig. 2c), similarly to $MoSi_2$ (Fig. 2a).

Fig. 3(a–e) show typical SEM secondary electron images of micropillar specimens, respectively of $MoSi_2$, $VSi_2$, $CrSi_2$, $NbSi_2$ and $TaSi_2$ after compression tests. All observations were made above the specimen along the direction inclined by 30 ° from the loading axis. For $MoSi_2$ (Fig 3a), relatively localized slip traces parallel to two equivalent {110} slip planes are clearly observed on both orthogonal side surfaces parallel to (01$\bar{7}$) and ($\bar{1}$00), indicating that the slip directions are not contained on either of the side surfaces. Although two different slip directions, 1/2<$\bar{1}$11> (magnitude: 4.53 Å, Schmid factor: 0.414) and [001] (magnitude: 7.85 Å, Schmid factor: 0.22) can be considered for slip on {110}, 1/2<$\bar{1}$11> must be the slip direction, because [001] is contained on the ($\bar{1}$00) side surface. The operation of {110}<$\bar{1}$11> slip was observed in $MoSi_2$ bulk single crystals in our previous studies [13], but the lowest temperature above which plastic flow by the operation of this slip was observed was 500 °C. This indicates that the temperature range for the operation of {110}<$\bar{1}$11> slip is extended, at least, down to room temperature by reducing the specimen size to the micron meter scale. In the same way, (0001)[$2\bar{1}\bar{1}0$] basal slip is identified to operate in all these four C40 TM disilicides with the [$2\bar{1}\bar{1}2$] loading orientation by slip trace analysis on two orthogonal surfaces as shown in Fig. 3(b–e). The operation of (0001)[$2\bar{1}\bar{1}0$] basal slip in [$2\bar{1}\bar{1}2$]-oriented specimens is consistent with what is observed for the respective bulk single crystals with the same orientation tested at high temperatures in our previous studies [16–18,20].

### 3.2. Dislocation structures

Two different deformation mechanisms (conventional shear and synchroshear) known to operate for the equivalent slip in $C11_b$ and C40 TM disilicides in the bulk form are briefly described, taking an example of (0001)[$2\bar{1}\bar{1}0$] basal slip in C40 TM disilicides [16–20]. Regardless of deformation mechanism, deformation is carried by dislocations with the Burgers vector (**b**) of 1/3[$2\bar{1}\bar{1}0$] dissociated into two identical collinear partial dislocations with **b** = 1/6[$2\bar{1}\bar{1}0$] with a stacking fault in between. The dissociation scheme of the 1/3[$2\bar{1}\bar{1}0$] dislocation is described as follows.

$$1/3\left[2\bar{1}\bar{1}0\right] \rightarrow 1/6\left[2\bar{1}\bar{1}0\right] + 1/6\left[2\bar{1}\bar{1}0\right]. \quad (1)$$

It is the $\mathbf{b}_1$ partial dislocation that is responsible for the conventional mechanism (Fig. S2a), while for the synchroshear mechanism, it is the $-\mathbf{b}_2$ and $-\mathbf{b}_3$ partial dislocations that move on adjacent (0001) basal planes synchronously to achieve the $\mathbf{b}_1$ shear as a whole (Fig. S2b). Our previous studies on respective bulk single crystals have confirmed that $VSi_2$, $NbSi_2$, $TaSi_2$ and $MoSi_2$ deform by conventional shear while $CrSi_2$ deforms by synchroshear [14,16–18,20]. In order to determine the deformation mechanism of the equivalent slip operated in the micropillar form at room temperature, we examine dislocation structures introduced in micropillar specimens of $CrSi_2$ and $NbSi_2$ as representatives that deform by synchroshear and conventional shear in the bulk crystals.

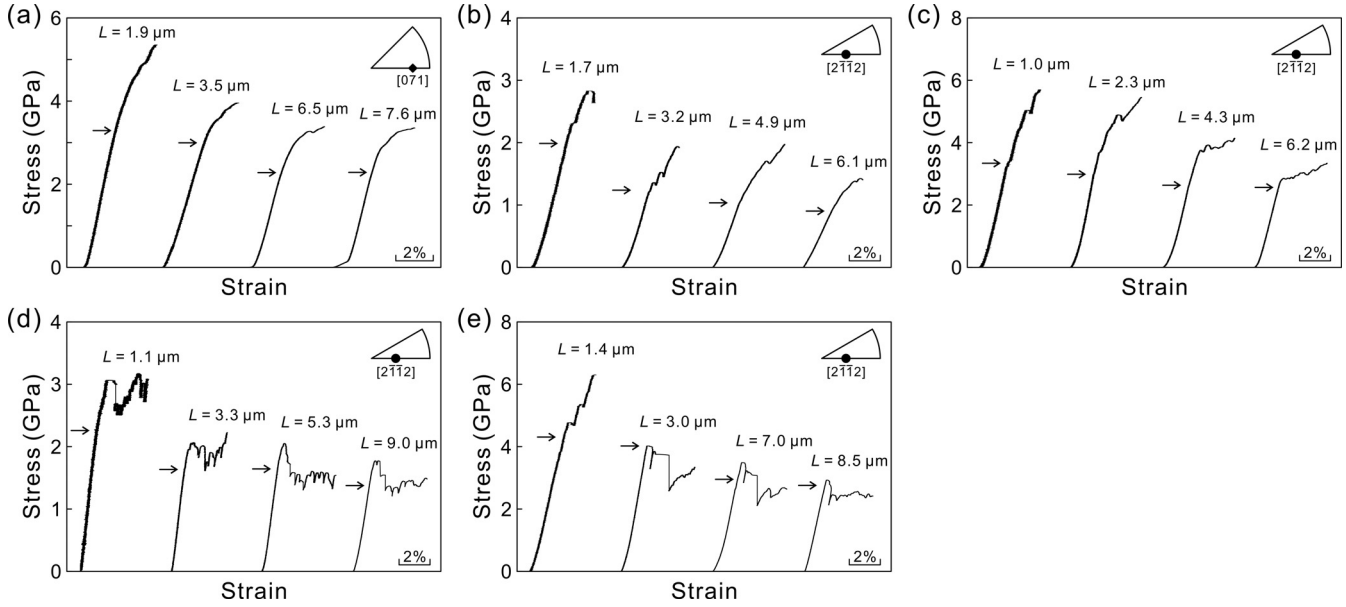


**Fig. 2.** Typical stress-strain curves obtained for micropillar specimens of (a) $MoSi_2$, (b) $VSi_2$, (c) $CrSi_2$, (d) $NbSi_2$ and (e) $TaSi_2$ with various specimen sizes. The compression-axis orientation and specimen sizes are indicated in each of the figures. Arrows in the figures indicate yield points estimated either from the elastic limit or from the stress at which the first strain bust occurs.

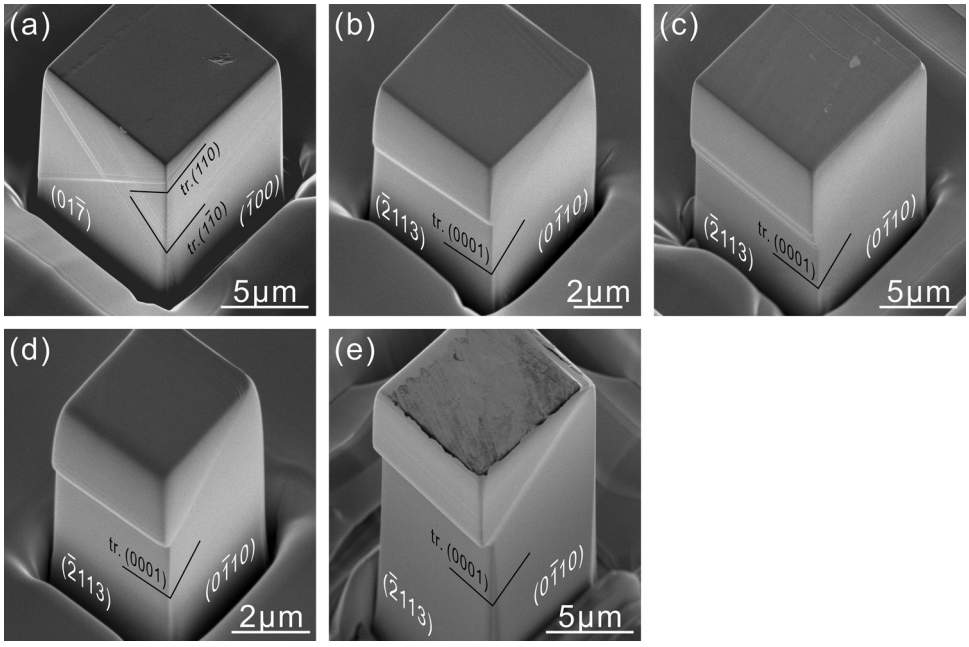


**Fig. 3.** Scanning electron microscopy images of (a) $MoSi_2$, (b) $VSi_2$, (c) $CrSi_2$, (d) $NbSi_2$ and (e) $TaSi_2$ single-crystal micropillar specimens after micropillar compression. The compression-axis orientation for $MoSi_2$ is [071] while it is [2$\bar{1}\bar{1}$2] for all other C40 TM disilides.

*3.2.1. $CrSi_2$*

Fig. 4a shows a weak-beam dark-filed (WBDF) image of dislocations with **b** = 1/3[2$\bar{1}\bar{1}$0] gliding on (0001) observed in a thin foil cut parallel to the ($\bar{2}$113) side surface of a [2$\bar{1}\bar{1}$2]-oriented micropillar specimen of $CrSi_2$ with $L$ = 7.2 $\mu$m. Not only dislocations but also many stacking faults (some of which are widely extended) are observed to be on (0001). 1/3[2$\bar{1}\bar{1}$0] dislocations tend to align mainly along either [$\bar{1}$2$\bar{1}$0] or [$\bar{1}\bar{1}$20], i.e. 60° from their Burgers vector direction. Each of 1/3[2$\bar{1}\bar{1}$0] dislocations is confirmed to dissociate into two identical collinear partials, because both partial dislocations are visible when imaged with **g** (reflection vector) = 2$\bar{1}\bar{1}$2 (Fig. 4b) and **g** = 1$\bar{2}$11 (Fig. 4d) are simultaneously invisible when imaged with **g** = 01$\bar{1}$0 (Fig. 4e) and **g** = 0003 (Fig. 4f). The dissociation scheme is consistent with that reported in our previous studies [16] as described in Eq. (1). These narrowly-dissociated dislocations exhibit an almost same separation distance consistently along the particular orientation such as 8.9 ± 1.0 nm for the 60 ° segment (average from 14 sampling points taken from two TEM specimens, the standard deviation was taken as an error). When this value is employed, the stacking fault energy is estimated to be 154 ± 20 mJ/m$^2$, using anisotropic energy factors calculated with elastic constants of $c_{11}$ = 372.2, $c_{33}$ = 385.2, $c_{12}$ = 45.3, $c_{13}$ = 82.6, $c_{44}$ = 149.1, $c_{66}$ = 163.5 GPa [39,40]. The stacking fault energy estimated in the present study is higher than that (114 ± 13 mJ/m$^2$) deduced from the separation distance for synchroshear partial dislocations in bulk single crystals [16]. Al-

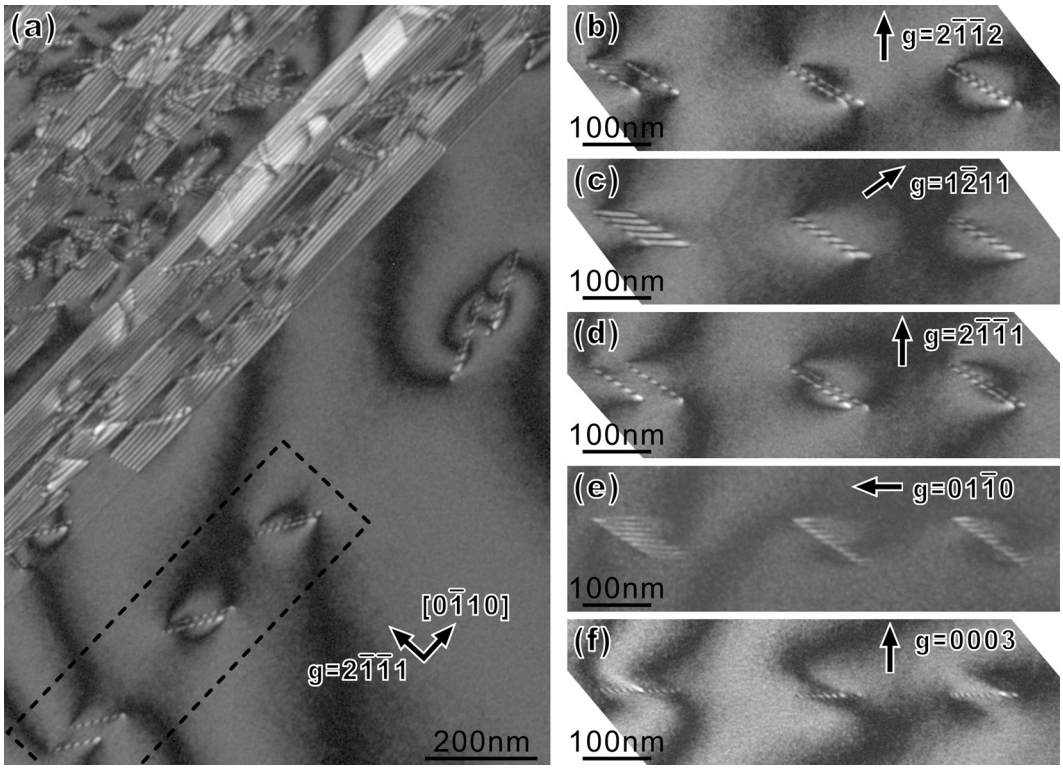


**Fig. 4.** (a) TEM deformation microstructure of $CrSi_2$ with the [2$\bar{1}\bar{1}$2] orientation ($L$ = 7.2 $\mu$m). (b–f) Weak-beam TEM contrast analysis of 1/3[2$\bar{1}\bar{1}$0] dislocations in the framed area in (a). Crystallographic directions and operating reflection vectors are indicated in each of the figures.

though the detailed analysis of the much widely-dissociated dislocations could not be made because of the extremely high density of stacking faults and dislocations in the regions containing widely-extended dislocations, the observed coexistence of narrowly- and widely-dissociated dislocations may suggest that the former were introduced initially (possibly from the specimen surface) and the latter were formed as a result that the movement of the trailing partials of the dissociated dislocations was impeded preferentially for some reason. A relatively strong interaction between dislocations gliding on neighboring glide planes may be responsible partly for blocking the movement of trailing partials, considering the fact that the much widely-extended stacking faults were observed only in a localized region where the glide deformation occurs intensively (upper part of Fig. 4a). Such coexistence of narrowly and widely-dissociated dislocations have not been observed in bulk specimens deformed at high temperatures. These characteristics of the deformation microstructure may imply that the stacking fault formed between two-coupled partial dislocations in the micropillar specimens is of different-type when compared to that formed between two-coupled synchroshear-partial dislocations in bulk specimens deformed at high temperatures and that the room-temperature deformation mechanism for (0001)[2$\bar{1}\bar{1}$0] basal slip in small specimens of the micrometer scale is different from that operative at high temperature in bulk specimens of the millimeter scale.

Fig. 5 shows an atomic-resolution high-angle annular dark-field (HAADF) STEM image of the core structure of a 1/3[2$\bar{1}\bar{1}$0] dislocation of edge character in a [2$\bar{1}\bar{1}$2]-oriented micropillar specimen of $CrSi_2$ with $L$ = 7.2 $\mu$m. The thin foil was cut parallel to the (0$\bar{1}$10) side surface of the [2$\bar{1}\bar{1}$2]-oriented micropillar specimen so that 1/3[2$\bar{1}\bar{1}$0] edge dislocations are observed end-on. Two partial dislocations are imaged at a separation distance of about 13.7 nm, being fairly consistent with that (9.1 $\pm$ 1.0 nm) estimated for pure edge segment using the stacking fault energy value of 154 $\pm$ 20 mJ/m$^2$ obtained by the WBDF TEM imaging. Construction of Burgers circuits around perfect and partial dislocations confirms that the Burgers vector of the perfect dislocation is **b** = 1/3[2$\bar{1}\bar{1}$0] and that the perfect dislocation dissociates into two partials with an identical Burgers vector of **b** = 1/6[2$\bar{1}\bar{1}$0], as show in Fig. 5a. An enlargement of the core region of the partial dislocation on the left-hand side of Fig. 5a confirms that the dislocation glide occurs between atomic layers A and B (Fig. 5b). In addition, the arrangement of bright spots in the stacking fault region between the two partial dislocations is identical to that in the undeformed region (without the stacking fault), indicating that shear deformation occurs along a single atomic layer in a conventional manner (as in bulk $VSi_2$, $NbSi_2$ and $TaSi_2$ [17,18,20]) but not synchronously along two adjacent atomic layer (as in bulk $CrSi_2$ [16]) through a synchroshear mechanism. This clearly indicates that the deformation mechanism for (0001)[2$\bar{1}\bar{1}$0] basal slip observed at room temperature for small specimens of $CrSi_2$ of the micrometer scale is different from that observed in bulk single crystals deformed at high temperatures above 800 °C.

Atomic-resolution HAADF STEM imaging further confirms that the core structure of the partial dislocation bounding a wider stacking fault (more than 30 nm) is the same as that observed in Fig. 5 and that shear deformation occurs similarly along a single atomic layer in a conventional manner. This means that the variation of the stacking fault width between the coupled partials does not originate from the difference in the deformation mechanism (conventional shear or synchroshear). The reason why the motion of the coupled partial dislocations is sometimes correlated and sometimes not correlated [41] has yet to be clarified.

### 3.2.2. $NbSi_2$

Fig. 6(a) shows a bright-field TEM image of dislocation structures introduced in a [2$\bar{1}\bar{1}$2]-oriented micropillar specimen of $NbSi_2$ with $L$ = 5.3 $\mu$m. The thin foil was cut parallel to the

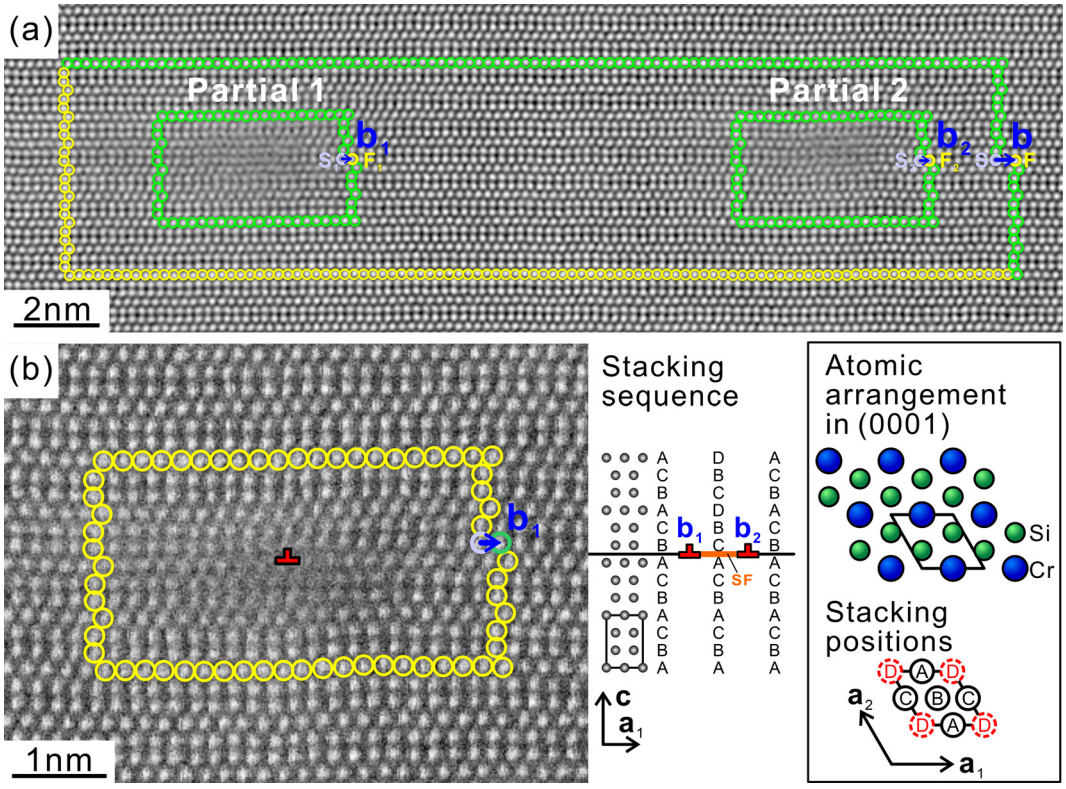


**Fig. 5.** (a) HAADF-STEM image of core structure of a 1/3[2$\bar{1}\bar{1}$0] edge dislocation introduced in [2$\bar{1}\bar{1}$2]-oriented micropillar of $CrSi_2$ with $L$ = 7.2 $\mu$m. (b) High-magnification image of core structure of the partial dislocation 1 in (a). The results of analysis of stacking order in the fault region between two partials are indicated in the bottom right.

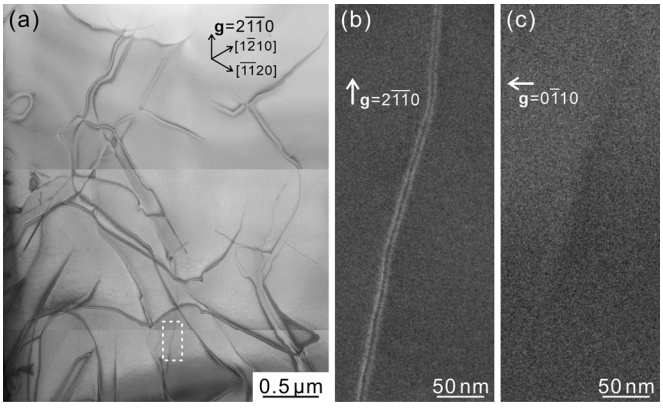


**Fig. 6.** (a) Bright-field TEM deformation microstructure and (b,c) weak-beam dark-filed TEM images (of the framed area in (a)) of micropillar $NbSi_2$ with the [2$\bar{1}\bar{1}$2] orientation ($L$ = 5.3 $\mu$m). Crystallographic directions and operating reflection vectors are indicated in each of the figures.

(0001) slip plane and most dislocations imaged are those with **b** = 1/3[2$\bar{1}\bar{1}$0] gliding on (0001). These dislocations do not have any strong tendency to align along a particular crystallographic orientation, although some weak tendency for the alignment along ⟨2$\bar{1}\bar{1}$0⟩ and ⟨01$\bar{1}$0⟩ is recognized. WBDF TEM contrast analysis indicates that each of 1/3[2$\bar{1}\bar{1}$0] dislocations dissociates into two identical collinear partials (Fig. 6b), as they are invisible when imaged with **g** = 0$\bar{1}$10 (Fig. 6c). The dissociation scheme is consistent with that reported in our previous studies of bulk crystals [17] as described in Eq. (1). The dissociation widths measured along the segments about 0°(screw), 17° and 90°(edge) from the Burgers vector are 5.2, 5.7 and 6.5 nm (Fig. 6b), from which the stacking fault energy is estimated to be 254 ± 10 mJ/m$^2$, using anisotropic energy factors calculated with elastic constants of $c_{11}$ = 380.2, $c_{33}$ = 468.0, $c_{12}$ = 75.9, $c_{13}$ = 88.3, $c_{44}$ = 145.3, $c_{66}$ = 152.2 GPa [39,40]. The estimated stacking fault energy is much smaller than that (397 mJ/m$^2$) we previously deduced from bulk single crystals deformed at high temperatures [17].

Fig. 7 shows an atomic-resolution HAADF STEM image of the core structure of a 1/3[2$\bar{1}\bar{1}$0] dislocation of edge character in a [2$\bar{1}\bar{1}$2]-oriented micropillar specimen of $NbSi_2$ with $L$ = 7.9 $\mu$m. The thin foil was cut parallel to the (0$\bar{1}$10) side surface of the [2$\bar{1}\bar{1}$2]-oriented micropillar specimen so that 1/3[2$\bar{1}\bar{1}$0] edge dislocations are observed end-on. Two partial dislocations are imaged at a separation distance of about 6.7 nm, which is consistent well with the separation distance for the dissociated edge dislocations observed by WBDF TEM (Fig. 6b). Burgers circuit construction around perfect and partial dislocations confirms that the Burgers vectors of the perfect and both partial dislocations are respectively, **b** = 1/3[2$\bar{1}\bar{1}$0] and **b** = 1/6[2$\bar{1}\bar{1}$0], as shown in Fig. 7a. An enlargement of the core region of the partial dislocation on the left-hand side of Fig. 7a confirms that the dislocation glide occurs between atomic layers C and A (Fig. 7b) and that the arrangement of bright spots in the stacking fault region between the two partial dislocations is identical to that in the undeformed region (without the stacking fault). This clearly indicates that shear deformation occurs along a single atomic layer in a conventional manner (as in bulk $VSi_2$, $NbSi_2$ and $TaSi_2$ [17,18]). The deformation mechanism for (0001)[ 2$\bar{1}\bar{1}$0] basal slip observed at room temperature for small specimens of $NbSi_2$ of the micron meter scale is conventional shear, exactly the same as that observed in bulk single crystals deformed at high temperatures above 500 °C.

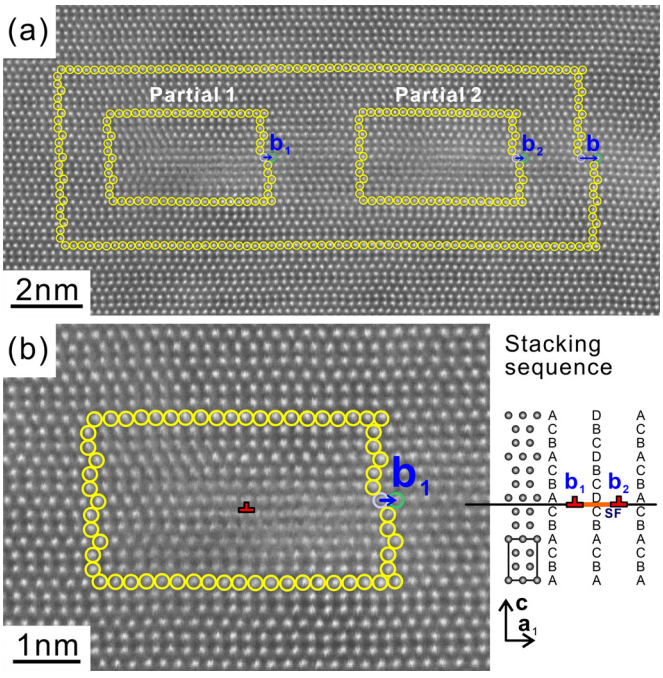


**Fig. 7.** (a) HAADF-STEM image of core structure of a 1/3[$2\bar{1}\bar{1}0$] edge dislocation introduced in [$2\bar{1}\bar{1}2$]-oriented micropillar of $NbSi_2$ with $L$ = 7.9 $\mu$m. (b) High-magnification image of core structure of the partial dislocation 1 in (a). The results of analysis of stacking order in the fault region between two partials are indicated in the bottom right.

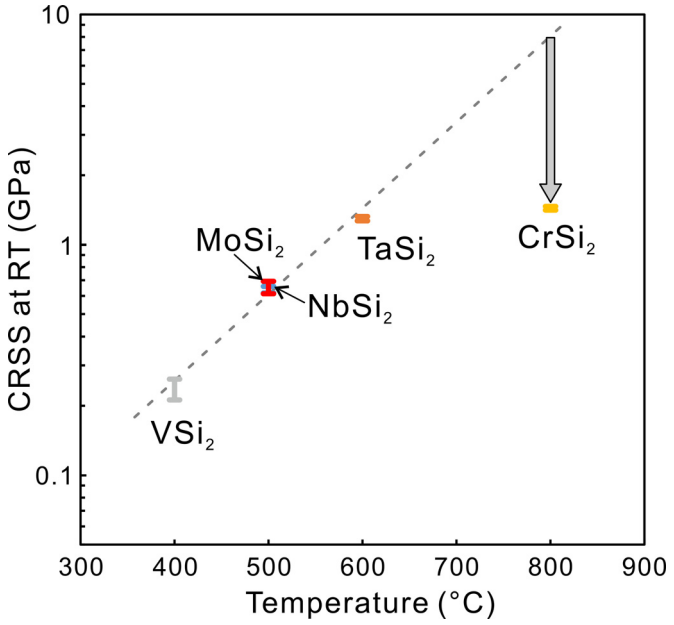


**Fig. 9.** Relationship between the extrapolated bulk CRSS values obtained from micropillar compression tests for $C11_b$ and C40 TM disilicides and the onset temperature for plastic flow of the corresponding bulk single crystals by the operation of their equivalent slip systems.

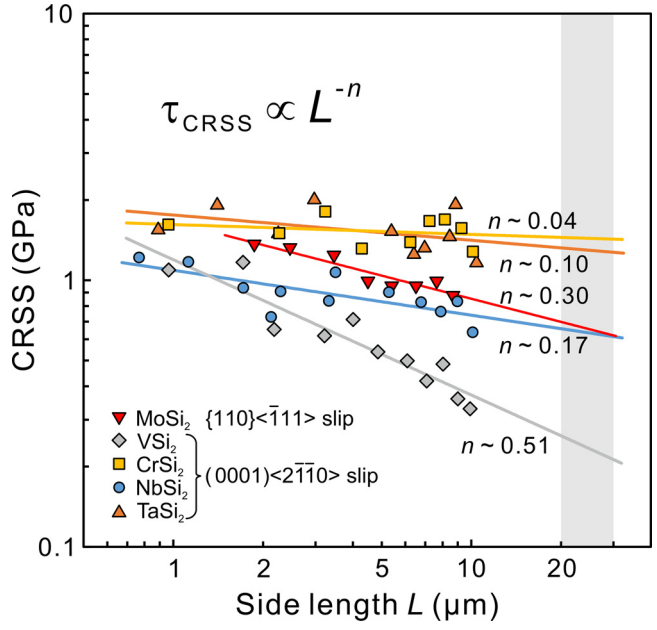


**Fig. 8.** (a) Specimen size dependence of CRSS for {110}<$\bar{1}$11> slip in $C11_b$–$MoSi_2$ and (0001)[ $2\bar{1}\bar{1}0$] slip in C40-$VSi_2$ , $CrSi_2$, $NbSi_2$ and $TaSi_2$.

## 4. Discussion

### 4.1. Size dependence of CRSS for equivalent slip systems

The values of CRSSs for {110}<$\bar{1}$11> slip in $C11_b$–$MoSi_2$ and (0001)[ $2\bar{1}\bar{1}0$] slip in C40-$VSi_2$ , $CrSi_2$, $NbSi_2$ and $TaSi_2$ calculated with the yield stress values and relevant Schmid factors are plotted in Fig. 8 as a function of specimen size (edge length $L$). The CRSS values exhibit an inverse power-law relationship with the specimen size, i.e., $\tau_{CRSS} \propto L^{-n}$, where $n$ is a power-law exponent. The $n$ value is known to be 0.2–0.5 or BCC (body-centered cubic) metals and 0.5–1.0 for FCC (face-centered cubic) metals [42–46]. The $n$ value is estimated for {110}<$\bar{1}$11> slip in $C11_b$–$MoSi_2$ is 0.30, which is close to those reported for BCC (body-centered cubic) metals (0.2–0.5) [42–46]. On the other hand, the $n$ values estimated for (0001)[ $2\bar{1}\bar{1}0$] slip in C40-$VSi_2$ , $CrSi_2$, $NbSi_2$ and $TaSi_2$ are 0.51, 0.04, 0.17 and 0.10, respectively. Except for $VSi_2$ that exhibits a very high $n$ value in the range of FCC metals, the $n$ values for the other three C40 TM disilicides are much smaller than those reported for conventional FCC and BCC metals [42–46].

The CRSS values obtained for micropillar specimens of most FCC and BCC metals are reported to coincide with the CRSS value obtained in bulk single crystals when the micropillar specimen size is in the range of about 20–30 $\mu$m [42,43]. Assuming that the same holds true for the CRSS values for the equivalent slip systems in $MoSi_2$ and C40-$TMSi_2$ (TM = V, Cr, Nb and Ta), the CRSS value at room temperature for the bulk crystal (hereafter, called the extrapolated bulk CRSS) is estimated by extrapolating the relevant power-law relationship to the specimen size of 20–30 $\mu$m. The extrapolated bulk CRSS values at room temperature thus estimated for {110}<$\bar{1}$11> slip in $MoSi_2$ and (0001)[ $2\bar{1}\bar{1}0$] slip in $VSi_2$, $CrSi_2$, $NbSi_2$ and $TaSi_2$ are 620 ± 40, 240 ± 20, 1440 ± 10, 640 ± 20 and 1300 ± 30 MPa, respectively.

Surprisingly, the extrapolated bulk CRSS values obtained from micropillar compression tests for these disilicides are exactly in the same order of the onset temperature for plastic flow of the corresponding bulk single crystals by the operation of their equivalent slip systems, as shown Fig. 9. The lower the extrapolated bulk CRSS value at room temperature is, the lower is the onset temperature for plastic flow. $CrSi_2$ is an exception for this relationship. This is obviously due to the fact that the deformation mechanism for (0001)[$2\bar{1}\bar{1}0$] equivalent slip changes from synchroshear in bulk to conventional shear in micropillars, as described in the Section 3.2.1. This will be discussed in more details in the next section.

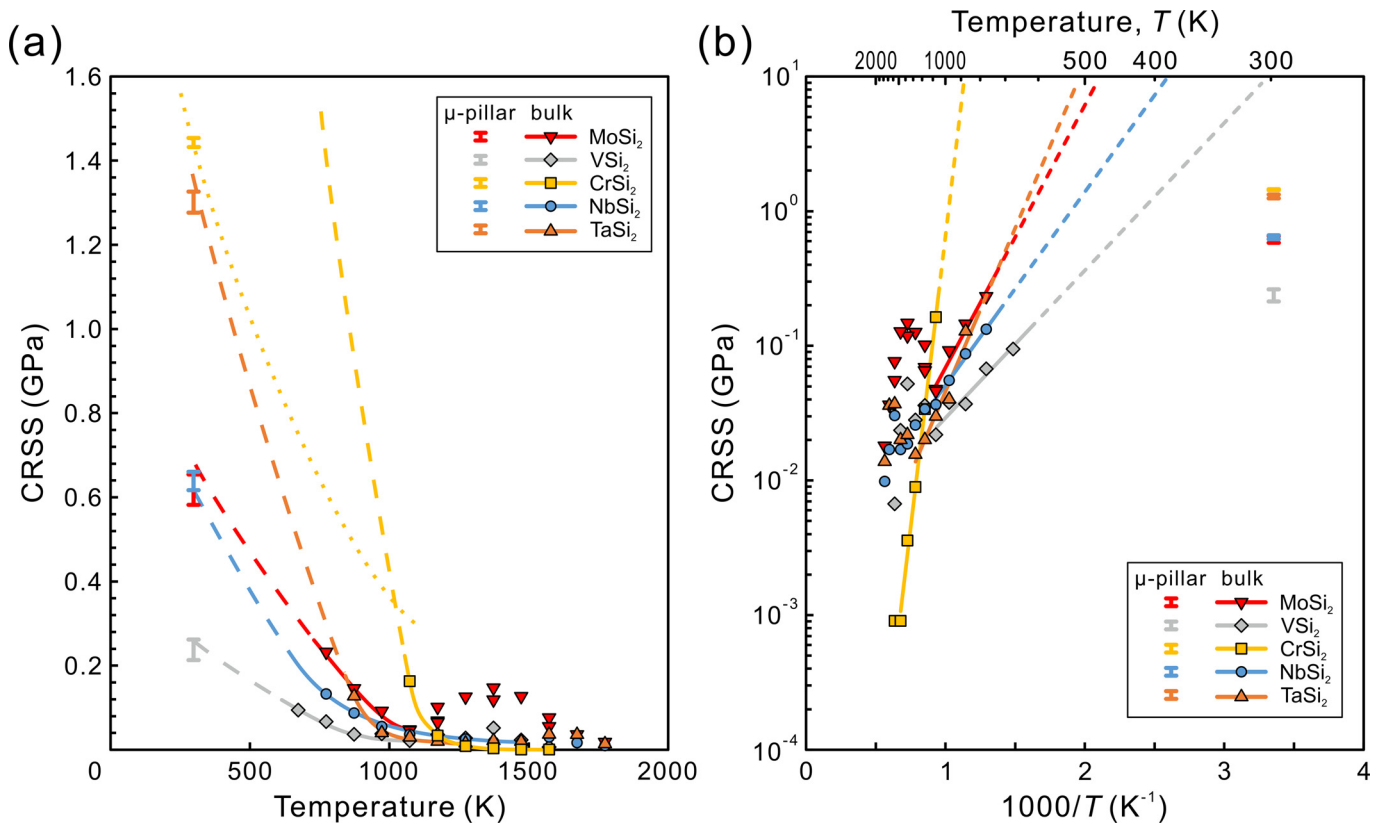


**Fig. 10.** Comparison of the bulk CRSS values at room temperature estimated by the extrapolation of the power-law relation with the temperature-dependent CRSS values obtained for the corresponding bulk single crystals of $C11_b$–$MoSi_2$ and C40 TM disilicides by high-temperature deformation [13,16–18]. (a) $\tau_{CRSS}$- $T$ plot and (b) $\ln(\tau_{CRSS})$-$(1/T)$ plot.

### 4.2. Comparison of CRSS values in bulk and micropillar forms

Fig. 10 compares these extrapolated bulk CRSS values at room temperature estimated by the extrapolation of the power-law relation with the temperature-dependent CRSS values obtained for the corresponding bulk single crystals of $C11_b$–$MoSi_2$ and C40 TM disilicides by high-temperature deformation [13,16–18,20]. Since yield stress anomaly is known to occur in the intermediate and higher temperature ranges as a result of Portevin-Le Chatelier effect in their bulk single crystals, the temperature-dependent CRSS values only in the low temperature range are considered as indicated with solid lines in Fig. 10a. For $CrSi_2$, the extrapolated bulk CRSS value (1440 ± 10 MPa) estimated from micropillar compression is much lower than that expected from the bulk single crystals deformed at high temperature. This is considered to reflect the fact that the deformation mechanism of $CrSi_2$ changes with decreasing temperature (from synchroshear to conventional shear) and indicates that the operation of (0001) $[2\bar{1}\bar{1}0]$ equivalent slip in a conventional manner is easier than that in a synchroshear mechanism for $CrSi_2$ at room temperature. The absence of conventional shear mechanism in high-temperature deformation of $CrSi_2$ bulk crystals implies that the temperature dependence of CRSS is much shallower for conventional shear mechanism (dotted line in Fig. 10a (an expected example)) than that for synchroshear mechanism in $CrSi_2$ (dashed line in Fig. 10a (extrapolated from high temperature data)). The occurrence of change in deformation mechanism with temperature has been similarly confirmed in some brittle materials such as SiC of the *6H* polytype by utilizing the micropillar compression method [38]. In contrast, both the extrapolated bulk CRSS values at room temperature estimated from micropillar compression and the high-temperature CRSS values obtained from bulk compression are expected to be plotted on a single monotonous curve for each of $C11_b$-$MoSi_2$ and C40 TM disilicides (except for $CrSi_2$) as shown with dashed lines in Fig. 10a, considering the fact that the deformation mechanism (conventional shear) does not change with temperature (as verified by TEM for $NbSi_2$ and considered also for the case for $MoSi_2$, $VSi_2$ and $TaSi_2$). Assuming that the strain rate $\dot{\gamma}$ can be expressed as a function of CRSS $\tau_{CRSS}$ and temperature $T$ with the equation of $\dot{\gamma} \propto \tau_{CRSS}^{m} \exp(-Q/kT)$, where $m$ is the stress exponent and $k$ is the Boltzman constant as in the case of various semiconducting materials [38,47], a linear relationship is expected between $\ln(\tau_{CRSS})$ and $(1/T)$ under constant strain rate deformation if the deformation mechanism does not change with temperature. Fig. 10b shows the $\ln(\tau_{CRSS})$- $(1/T)$ plots for $C11_b$–$MoSi_2$ and C40 TM disilicides (strain rate: $\sim 10^{-4}$/s). The bulk CRSS values at room temperature estimated from micropillar compression for all TM disilicides tested in this study are found to be much lower than those extrapolated from the high-temperature CRSS values, although the slopes for $C11_b$–$MoSi_2$ and C40-$VSi_2$, $NbSi_2$ and $TaSi_2$, which deform by a conventional shear mechanism in the whole temperature range, are much more gradual than that for $CrSi_2$ exhibiting the transition of deformation mechanism with temperature. This may suggests that the dominant controlling factor for the room-temperature CRSS values of $C11_b$-$MoSi_2$ and C40-$VSi_2$, $NbSi_2$ and $TaSi_2$ is also different from that at high temperatures, even though the deformation mechanism does not change with temperature. However, the reason for the discrepancy of the room-temperature CRSS values for $C11_b$-$MoSi_2$ and C40-$VSi_2$, $NbSi_2$ and $TaSi_2$ estimated by the two different methods remains to be clarified.

## 5. Conclusions

We investigate the room-temperature deformation behavior of single crystals of $C11_b$–$MoSi_2$ and C40-$VSi_2$, $CrSi_2$, $NbSi_2$ and $TaSi_2$ by micropillar compression as a function of specimen size. The results obtained are summarized as follows.

(1) All TM disilicides exhibit plastic flow by the operation of equivalent slip ($\{110\}\langle\bar{1}11\rangle$ and $(0001)\langle 2\bar{1}\bar{1}0\rangle$, respectively, for the $C11_b$ and C40 structures) even at room temperature in the micropillar form, in contrast to the high onset temperature for plastic flow in the bulk form. For all TM disilicides, the CRSS values exhibit an inverse power-law relationship with the specimen size. The power-law exponents for these TM disilicides are generally much smaller than those reported for conventional FCC and BCC metals.

(2) The bulk CRSS values at room temperature for $\{110\}\langle\bar{1}11\rangle$ slip in $MoSi_2$ and $(0001)[2\bar{1}\bar{1}0]$ slip in $VSi_2$, $CrSi_2$, $NbSi_2$ and $TaSi_2$ are 620 ± 40, 240 ± 20, 1440 ± 10, 640 ± 20 and 1300 ± 30 MPa, respectively, when estimated from the size-dependent CRSS values in micropillar compression. The extrapolated bulk CRSS values at room temperature are exactly in the same order of the onset temperature for plastic flow of the corresponding bulk single crystals by the operation of their equivalent slip systems.

(3) The extrapolated bulk CRSS value at room temperature does not coincide with that estimated from the temperature-dependent CRSS values obtained for the corresponding bulk single crystals by high-temperature deformation when deformation mechanism changes with temperature (from synchroshear to conventional shear) as verified for $CrSi_2$.

## Declaration of Competing Interest

The authors declare that they have no known competing financial interests or personal relationships that could have appeared to influence the work reported in this paper.

## Acknowledgments

This work was supported by Japan Society for the Promotion of Science (JSPS) KAKENHI Grant Nos. JP18H05478, JP18H05450, JP18H05451, JP19H00824, JP20K21084, JP21H01651, the Elements Strategy Initiative for Structural Materials (ESISM) from the Ministry of Education, Culture, Sports, Science and Technology (MEXT) of Japan (Grant No. JPMXP0112101000), in part by Japan Science and Technology Agency (JST)ALCA (Grant No. JPMJAL1004) and JST CREST (Grant No. JPMJCR1994).

## References

[1] A.K. Vasudevan, J.J. Petrovic, A comparative overview of molybdenum disilicide composites, Mater. Sci. Eng. A 155 (1992) 1–17.
[2] D.M. Shah, D. Berczik, D.L. Anton, R. Hecht, Appraisal of other silicides as structural materials, Mater. Sci. Eng. A 155 (1992) 45–57.
[3] J.J. Petrovic, A.K. Vasudevan, Key developments in high temperature structural silicides, Mater. Sci. Eng. A 261 (1999) 1–5.
[4] M. Yamaguchi, H. Inui, K. Ito, High-temperature structural intermetallics, Acta Mater. 48 (2000) 307–322.
[5] R. Mitra, Mechanical behavior and oxidation resistance of structural silicides, Int. Mater. Rev. 51 (2006) 13–64.
[6] P. Villars, L.D. Calvert, Pearson's Handbook of Crystallographic Data for Intermetallic Phases, American Society for Metals, Metals Park, 1985.
[7] H. Inui, A. Fujii, K. Tanaka, H. Sakamoto, K. Ishizuka, New electron diffraction method to identify the chirality of enantiomorphic crystals, Acta Cryst. B 59 (2003) 802–810.
[8] H. Sakamoto, A. Fujii, K. Tanaka, H. Inui, Enantiomorph identification of transition-metal disilicides with the C40 structure (the space group of $P6_222$ and $P6_422$) by new convergent-beam electron diffraction method, Acta Mater. 53 (2005) 41–52.
[9] S. Fujio, K. Tanaka, H. Inui, Formation probability for enantiomorphic crystals (with the spave groups of $P6_222$ and $P6_422$) in transition-metal disilicides with the C40 structure as determined by convergent-beam electron diffraction, Intermetallics 15 (2007) 245–252.
[10] Y. Umakoshi, T. Nakashima, T. Yamane, H. Senba, O. Izumi, Plastic deformation of transition metal silicides with the $C11_b$ and the C40 structure, in: Proceedings of the 6th JIM International Symposium on Intermetallic Compounds, Structure and Mechanical properties, Japan Institute Metals, Sendai, 1991, pp. 639–643.
[11] Y. Umakoshi, T. Nakashima, T. Nakano, E. Yanagisawa, Plastic behavior and deformation structure of silicide single crystals with transition metals at high temperatures, Mater. Res. Soc. Symp. Proc. 322 (1994) 9–20.
[12] S.A. Maloy, A.H. Heuer, J.J. Lewandowski, T.E. Mitchell, On the slip systems in $MoSi_2$, Acta Metall. Mater. 40 (1992) 3159–3165.
[13] K. Ito, H. Inui, Y. Shirai, M. Yamaguchi, Plastic deformation of $MoSi_2$ single crystals, Philos. Mag. A 72 (1995) 1075–1097.
[14] K. Ito, T. Yano, T. Nakamoto, H. Inui, M. Yamaguchi, Plastic deformation of $MoSi_2$ and $WSi_2$ single crystals and directionally solidified $MoSi_2$-based alloys, Intermetallics 4 (1996) S119–S131.
[15] H. Inui, K. Ishikawa, M. Yamaguchi, Effects of alloying elements on plastic deformation of single crystals of $MoSi_2$, Intermetallics 8 (2000) 1131–1145.
[16] H. Inui, M. Moriwaki, S. Ando, M. Yamaguchi, Plastic deformation of single crystals of $CrSi_2$ with the C40 structure, Mater. Sci. Eng. A 239–240 (1997) 63–68.
[17] M. Moriwaki, K. Ito, H. Inui, M. Yamaguchi, Plastic deformation of single crystals of $NbSi_2$ with the C40 structure, Mater. Sci. Eng. A 239–240 (1997) 69–74.
[18] H. Inui, M. Moriwaki, M. Yamaguchi, Plastic deformation of single crystals of $VSi_2$ and $TaSi_2$ with the C40 structure, Intermetallics 6 (1998) 723–728.
[19] H. Inui, M. Moriwaki, K. Ito, M. Yamaguchi, Plastic deformation of single crystals of $Mo(Si, Al)_2$ with the C40 structure, Philos. Mag. A 77 (1998) 375–394.
[20] H. Inui, M. Yamaguchi, Deformation mechanisms of transition-metal disilicides with the hexagonal C40 structure, Intermetallics 9 (2001) 857–862.
[21] W.W. Gerberich, J. Michler, W.M. Mook, R. Ghisleni, F. Östlund, D.D. Stauffer, R. Ballarini, Scale effects for strength, ductility, and toughness in "brittle" materials, J. Mater. Res. 24 (2009) 898–906.
[22] F. Östlund, K. Rzepiejewska-Malyska, K. Keifer, L.M. Hale, Y. Tang, R. Ballanini, W. Gerberich, J. Michler, Brittle-to-ductile transition in uniaxial compression of silicon pillars at room temperature, Adv. Funct. Mater. 19 (2009) 2439–2444.
[23] T.H. Sung, J.C. Huang, J.H. Hsu, S.R. Jian, Mechanical response of GaN film and micropillar under nanoindentation and microcompression, Appl. Phys. Lett. 97 (2010) 171904.
[24] F. Östlund, P.R. Howie, R. Ghisleni, S. Korte, K. Leifer, W.J. Clegg, J. Michler, Ductile-brittle transition in micropillar compression of GaAs at room temperature, Philos. Mag. 91 (2011) 1190–1199.
[25] S. Korte, W.J. Clegg, Discussion of the dependence of the effect of size on the yield stress in hard materials studied by microcompression of MgO, Philos. Mag. 91 (2011) 1150–1162.
[26] S. Korte-Kerzel, Microcompression of brittle and anisotropic crystals: recent advances and current challenges in studying plasticity in hard materials, MRS Commun. 7 (2017) 109–120.
[27] S. Nakatsuka, K. Kishida, H. Inui, Micropillar compression of $MoSi_2$ single crystals, MRS Symp. Proc. 1760 (2015) 1760 mrsf14–yy05-09.
[28] K. Kishida, T. Maruyama, H. Matsunoshita, T. Fukuyama, H. Inui, Micropillar compression deformation of single crystals of $Mo_5SiB_2$ with the tetragonal $D8_l$ structure, Acta Mater. 159 (2018) 416–428.
[29] K. Kishida, T. Fukuyama, T. Maruyama, H. Inui, Room temperature deformation of single crystals of $Ti_5Si_3$ with the hexagonal $D8_8$ structure investigated by micropillar compression tests, Sci. Rep. 10 (2020) 17983.
[30] K. Kishida, T. Maruyama, T. Fukuyama, H. Inui, Micropillar compression deformation of single crystals of $\alpha$-$Nb_5Si_3$ with the $D8_l$ structure, Sci. Tech. Adv. Mater. 21 (2021) 805–816.
[31] Z. Chen, B. Paul, S. Majumdar, N.L. Okamoto, K. Kishida, H. Inui, S. Otani, Room-temperature deformation of single crystals of $ZrB_2$ and $TiB_2$ with the hexagonal $AlB_2$ structure investigated by micropillar compression, Sci. Rep. 11 (2021) 14256.
[32] N.L. Okamoto, D. Kashioka, M. Inomoto, H. Inui, H. Takebayashi, S. Yamaguchi, Compression deformability of Γ and $\zeta$ Fe-Zn intermetallics to mitigate detachment of brittle intermetallic coating of galvannealed steels, Scr. Mater. 69 (2013) 307–310.
[33] N.L. Okamoto, M. Inomoto, H. Adachi, H. Takebayashi, H. Inui, Micropillar compression deformation of single crystals of the intermetallic compound $\zeta$-$FeZn_{13}$, Acta Mater. 65 (2014) 229–239.
[34] Y. Hashizume, M. Inomoto, H. Takebayashi, N.L. Okamoto, H. Inui, Micropillar compression deformation of single crystals of the intermetallic compound Γ-$Fe_4Zn_9$, Acta Mater. 199 (2020) 514–522.
[35] Y. Hashizume, M. Inomoto, N.L. Okamoto, H. Inui, Plastic deformation of single crystals of the $\delta_{1p}$ and $\delta_{1k}$ intermetallic compounds in the Fe-Zn System by micropillar compression, Int. J. Plast. 136 (2021) 102889.
[36] K. Kishida, M. Okutani, H. Inui, Direct observation of zonal dislocation in complex materials by atomic-resolution scanning transmission electron microscopy, Acta Mater. submitted.
[37] M. Higashi, S. Momono, K. Kishida, N.L. Okamoto, H. Inui, Anisotropic plastic deformation of single crystals of the MAX phase compound $Ti_3SiC_2$ investigated by micropillar compression, Acta Mater. 161 (2018) 161–170.

[38] K. Kishida, Y. Shinkai, H. Inui, Room temperature deformation of 6*H*-SiC single crystals investigated by micropillar compression, Acta Mater. 187 (2020) 19–28.
[39] M.M. Savin, V.M. Chernov, A.M. Strokova, Energy factor of dislocations in hexagonal crystals, Phys. Stat. Sol. 35 (1976) 747–754 (a).
[40] F. Chu, M. Lei, S.A. Maloy, J.J. Petrovic, T.E. Mitchell, Elastic properties of C40 transition metal disilicides, Acta mater. 44 (1996) 3035–3048.
[41] S. Takeuchi, Glide of interacting partial dislocations in the Peierls mechanism, Philos. Mag. A 71 (1995) 1255–1263.
[42] D.M. Dimiduk, M.D. Uchic, T.A. Parthasarathy, Size-affected single-slip behavior of pure nickel microcrystals, Acta Mater. 53 (2005) 4065–4077.
[43] M.D. Uchic, P.A. Shade, D.M. Dimiduk, Plasticity of micrometer-scale single crystals in compression, Annu. Rev. Mater. Res. 39 (2009) 161–186.
[44] K.S. Ng, A.H.W. Ngan, Breakdown of Schmid's law in micropillars, Scr. Mater. 59 (2008) 796–799.
[45] A.S. Schneider, D. Kaufmann, B.G. Clark, C.P. Frick, P.A. Gruber, R. Mönig, O. Kraft, E. Arzt, Correlation between critical temperature and strength of small-scale bcc pillars, Phys. Rev. Lett. 103 (2009) 105501.
[46] S.W. Lee, W.D. Nix, Size dependence of the yield strength of fcc and bcc metallic micropillars with diameters of a few micrometers, Philos. Mag. 92 (2012) 1238–1260.
[47] S. Fujita, K. Maeda, S. Hyodo, Dislocation glide motion in 6H SiC single crystals subjected to high-temperature deformation, Philos. Mag. A 55 (1987) 203–215.